The cochlear outer hair cell speed paradox

Richard D. Rabbitt[a,1] (ID)

[a]Biomedical Engineering, Otolaryngology, and Neuroscience Program, University of Utah, Salt Lake City, UT 84112

Cochlear outer hair cells (OHCs) are among the fastest known biological motors and are essential for high-frequency hearing in mammals. It is commonly hypothesized that OHCs amplify vibrations in the cochlea through cycle-by-cycle changes in length, but recent data suggest OHCs are low-pass filtered and unable to follow high-frequency signals. The fact that OHCs are required for high-frequency hearing but appear to be throttled by slow electromotility is the "OHC speed paradox." The present report resolves this paradox and reveals origins of ultrafast OHC function and power output in the context of the cochlear load. Results demonstrate that the speed of electromotility reflects how fast the cell can extend against the load, and does not reflect the intrinsic speed of the motor element itself or the nearly instantaneous speed at which the coulomb force is transmitted. OHC power output at auditory frequencies is revealed by emergence of an imaginary nonlinear capacitance reflecting the phase of electrical charge displacement required for the motor to overcome the viscous cochlear load.

prestin | electromotility | capacitance | piezoelectricity | temperature

The cochlea endows mammals with the ability to hear sounds over a frequency range far surpassing the capability of other vertebrate classes. Superior performance has primary origins in the function of outer hair cells (OHCs), which are uniquely electromotile and respond to a change in voltage with change in length (1). OHCs are ultrafast under some conditions, capable of generating forces at frequencies exceeding 80 kHz (2). The motor mechanism requires expression of the protein prestin in the lateral wall membrane (3), which imparts OHCs with properties similar to piezoelectric materials where the electric field generates a coulomb force that drives charge displacement and concomitant mechanical strain on a cycle-by-cycle basis (4, 5). The idea of cycle-by-cycle amplification at auditory frequencies has been challenged by recent experimental evidence that OHC membranes exhibit low-pass characteristics (6, 7). Precisely how OHCs circumvent low-pass characteristics and provide power to the cochlea at high auditory frequencies is the primary subject of the present report.

OHCs sense sound through mechano-electrical transduction (MET) channels that open cycle-by-cycle in response to sound-induced displacement of their apical stereocilia (8). The MET current entering the cell is modulated at auditory frequencies and drives changes in intracellular voltage. Like all cells, OHC membranes have electrical capacitance, which reduces the voltage modulation as the sound frequency is increased above the membrane RC corner frequency (RC: resistance times capacitance). The RC corner is unusually high in OHCs owing to a standing K^+ conductance in the membrane (9). Ultrafast K^+ channel gating might also play a role in extending the effective RC (10). Evidence that OHCs can modulate voltage at auditory frequencies is compelling, but whether or not the motor mechanism can be driven by voltage cycle-by-cycle is less clear. Direct experimental measurement of electrical charge displacement and motility in OHCs and membrane patches suggests prestin-dependent electromotility is too slow to support cycle-by-cycle amplification (6, 11–13).

The present report is focused on high-frequency power output of OHCs and applies a thermodynamic approach to examine whole-cell function. Results demonstrate the OHC speed paradox arises in part from the misleading nature of conventional capacitance recordings and the relationship between charge displacement and OHC power output under load. The paradox is resolved by accounting for the reversible interplay between charge displacement, voltage, stress, and temperature using first principles set forth by Maxwell, Seebeck, Currie, and Newton. Results explain high-frequency force generation in isolated OHCs (2), low-pass nonlinear capacitance (NLC) in membrane patches (13), and OHC power output in the cochlea across the frequency bandwidth of hearing. Fundamental mechanisms are revealed through examination of load-dependent electrical charge displacement in the piezoelectric membrane complex. The same principles are shown to explain the origins of infrared laser-induced charge displacement in hair cells, neurons, and model membranes (14, 15).

Results

Capacitance Susceptibility. Isolated OHCs exhibit a signature voltage-dependent capacitance reflecting reversible electromechanical charge displacement in the membrane. Examining the origin of NLC provides insight into how OHCs function in the cochlea. OHC membranes are complex inhomogeneous mixtures of lipids, proteins, and charged macromolecules, bordered on each side by ionic double layers and membrane-associated macromolecules. From an experimental point of view, it is generally impossible to directly control or measure the nanoscale distribution of charge associated with the membrane, but straightforward to experimentally control the total voltage drop across the membrane V, the temperature Θ, and the stress T_i ($i = 1,2,3$). For small perturbations about the resting state (V_0, Θ_0, T_{i0}), the chain rule of calculus provides the electrical displacement current I_D across the membrane in terms of the charge Q:

Significance

Mammalian hearing requires outer hair cells for amplification and tuning in the cochlea. The amplification process works at frequencies at least 10 times higher than might be expected based on electrical properties of the cells. The present report demonstrates how protein-dependent membrane piezoelectricity underlies high-frequency function, and why power output is maximum at frequencies much higher than would be predicted based on traditional experimental measurements. The interplay between electrical charge displacement and mechanical strain in the membrane motor is key. The same biophysical principles identify the origins of infrared laser-induced capacitive currents reported previously in hair cells, HEK cells, and neurons.

$$I_D = \frac{dQ}{dt} = C_E \frac{\partial V'}{\partial t} + C_\Theta \frac{\partial \Theta'}{\partial t} + C_{Ti} \frac{\partial T_i'}{\partial t}. \qquad [1]$$

The capacitance voltage susceptibility is $C_E = \partial Q/\partial V'$ (electric Maxwell effect, farad, coulomb·volt^{-1}), capacitance temperature susceptibility is $C_\Theta = \partial Q/\partial \Theta'$ (thermal Seebeck effect, coulomb·°C^{-1}), and the capacitance stress susceptibility is $C_{Ti} = \partial Q/\partial T_i'$ (piezoelectric Currie effect, coulomb·meter^2·newton^{-1}). Einstein's summation convention applies for repeated indices. Capacitance susceptibilities describe the charge displacement driven by small perturbations in each of the three thermodynamic state variables; they are thermodynamically independent but related to each other by reciprocity, e.g., $\partial^2 Q/\partial V' \partial \Theta' = \partial^2 Q/\partial \Theta' \partial V'$ requires $\partial C_E/\partial \Theta' = \partial C_\Theta/\partial V'$. The term "susceptibility" is used here to distinguish values from idealized capacitor theory (16). Measurements of cell membrane capacitance often assume $dQ/dt = C_m(\partial V'/\partial t)$ and report C_m as "electrical capacitance," but this approach can be misleading for piezo- or thermo-electric membranes because stress and/or temperature can change with voltage, coupling multiple terms in Eq. **1**. The role OHCs in the cochlea is to convert electrical power into mechanical power, requiring OHC membranes to invoke capacitance voltage susceptibility C_E and capacitance stress susceptibility C_{Ti} at the same time. Results in the present report demonstrate how these two terms interact to enable OHC power output at auditory frequencies.

The capacitance susceptibilities in Eq. **1** arise from first principles of thermodynamics, and can be described agnostic to the specific molecular origins. All results in the present report are based on general thermo-piezoelectric materials where the electromechanical properties are determined from derivatives of the Gibbs free energy. The standard second order theory is used to describe thermo-electromechanics of nonexcitable membrane domains (17, 18) and a nonlinear extension is used to describe thermo-piezo-electromechanics of excitable domains (*SI Appendix, A*). The two domains are configured in parallel electrically and in series mechanically.

Capacitance Voltage Susceptibility in OHCs. The capacitance voltage susceptibility C_E in OHCs arises from the addition of voltage-driven charge displacement in the passive membrane domains (linear capacitance: C_E^L), plus voltage-driven charge displacement in piezoelectric domains [NLC: $C_E^P = C_E^{pk} f(\xi)$]. Holding stress and temperature constant, the total capacitance voltage susceptibility is as follows:

$$C_E = C_E^L + C_E^{pk} f(\xi). \qquad [2]$$

The standard electrostriction form $C_E^L \approx C_E^0(1 + a_2(V + \psi)^2)$ is used for the passive domain (19) (*SI Appendix,* Eq. **C4** and Fig. **S1**), where $C_E^0 = A^L \varepsilon/h^L$, ε is the electrical permittivity, A^L is the area of the passive domain, and h^L is the thickness. A small voltage dependence arises from the electrostriction parameter a_2 and spontaneous polarization ψ. The increased linear capacitance present in OHCs at hyperpolarized voltages is not included in the present analysis. The piezoelectric capacitance susceptibility in Eq. **2** arising from the motor domains $C_E^p = C_E^{pk} f(\xi)$ is highly nonlinear (*SI Appendix,* Eq. **A6**). C_E^{pk} is the peak NLC voltage susceptibility occurring at voltage V^{pk} (at resting temperature and stress) arising from the piezoelectric coefficients, the motor domain compliance tensor, and the area of the motor domain. The nonlinearity $f(\xi)$ describes strain-dependent saturation of the piezoelectric charge displacement as a function of thermodynamic state of the membrane (V_0, T_{i0}, Θ_0'). Saturation arises from prestin extending from its fully contracted configuration to its fully extended configuration, and hence is directly dependent on strain in the motor domain.

Dependence on strain makes C_E^p dependent on all three state variables: voltage, force, and temperature. Specifically, the argument of f is proportional to strain and written $\xi = (V - V^{pk} + \beta_F F' + \beta_\Theta \Theta') \lambda^{-1}$, where β_Θ is the temperature sensitivity and β_F is axial force sensitivity. (Note: the force term $\beta_F F'$ is a simplified one-dimensional version of $\beta_{Ti} T_i'$ and, by Laplace's law at low frequencies, can alternatively be written in terms of intracellular pressure $\beta_P P'$ and load.) The charge sensitivity is $\lambda = k_B \Theta/ze$, where Θ is absolute temperature, k_B is Boltzmann's constant, ze is the maximum charge movement between saturated extended and contracted states. In the present report, $f(\xi)$ is approximated using the first derivative of the Langevin function, so $f(\xi) = 3f_0((1/\xi^2) - Csch(\xi)^2)$, where the temperature scaling factor is $f_0 = \Theta/\Theta_0$. A Langevin function is used here with the recognition that prestin conformational changes likely involve multiple transition states (20), resulting in broader tails in the voltage-displacement curve than would be predicted by a simple two-state Boltzmann, but use of an alternative functional form does not change conclusions of the present report related to the OHC speed paradox.

To establish confidence in the thermo-piezoelectric description, the capacitance voltage susceptibility C_E from Eq. **2** is compared to data from isolated OHCs in Fig. 1 (model parameters are listed in Table 1). Unlike most cells, piezoelectric capacitance voltage susceptibility C_E^P introduces a strong voltage dependence in OHCs that can double the capacitance at voltage V^{pk}. Theoretical predictions (solid curves) are compared to data from Kakehata and Santos-Sacchi (21) at two different intracellular pressures in Fig. 1 *A* and *B* and to data from Santos-Sacchi and Huang (22) at three different temperatures in Fig. 1 *C* and *D*. It should be noted that the data in Fig. 1 *C* and *D* (22) are shifted relative to OHCs in the cochlea where V^{pk} is closer to the cell resting potential of −40 to −50 mV (9). An increase in intracellular pressure shifts the nonlinear piezoelectric capacitance to the right without a detectable change in f_0 or λ, while an increase in temperature shifts the NLC to the right while increasing both f_0 and λ. All curves in Fig. 1*C* use the same value of C_E^{pk}, and the shift in magnitude and voltage dependence arises naturally from temperature dependence of $f(\xi)$, not from any change in constitutive parameters.

Capacitance Stress Susceptibility in OHCs. The capacitance stress susceptibility arises from the piezoelectric domains and determines the charge displacement for small perturbations in membrane stress $C_{Ti}(\partial T_i/\partial t)$, axial force $C_F(\partial F/\partial t)$, or intracellular pressure $C_P(\partial P/\partial t)$ (*SI Appendix,* A). To facilitate comparison to experimental data, the capacitance pressure susceptibility $C_P = \partial Q^P/\partial P$ is as follows:

$$C_P = C_E^{pk} \beta_P f(\xi), \qquad [3]$$

and is shown as a function of voltage in Fig. 1*E*. $C_P \to 0$ at highly hyperpolarized and depolarized voltages, and peaks at V^{pk}. The significance of C_P is that it determines the electrical displacement current evoked by a change in intracellular pressure, $I_{DP} = C_P(\partial P/\partial t)$ [which can be converted to displacement current induced by a change in axial force $I_{DF} = C_F(\partial F/\partial t)$ or membrane stress $I_{DT} = C_{Ti}(\partial T_i/\partial t)$]. Under dynamic load, the stress-induced charge displacement interacts with the voltage-induced change displacement on a cycle-by-cycle basis. This interaction provides feedback, where the active piezoelectric element responds to both the load and voltage.

Capacitance Temperature Susceptibility. The capacitance temperature susceptibility C_Θ arises from both the passive and piezoelectric domains, and determines the charge displacement for small perturbations in membrane temperature. In OHCs,
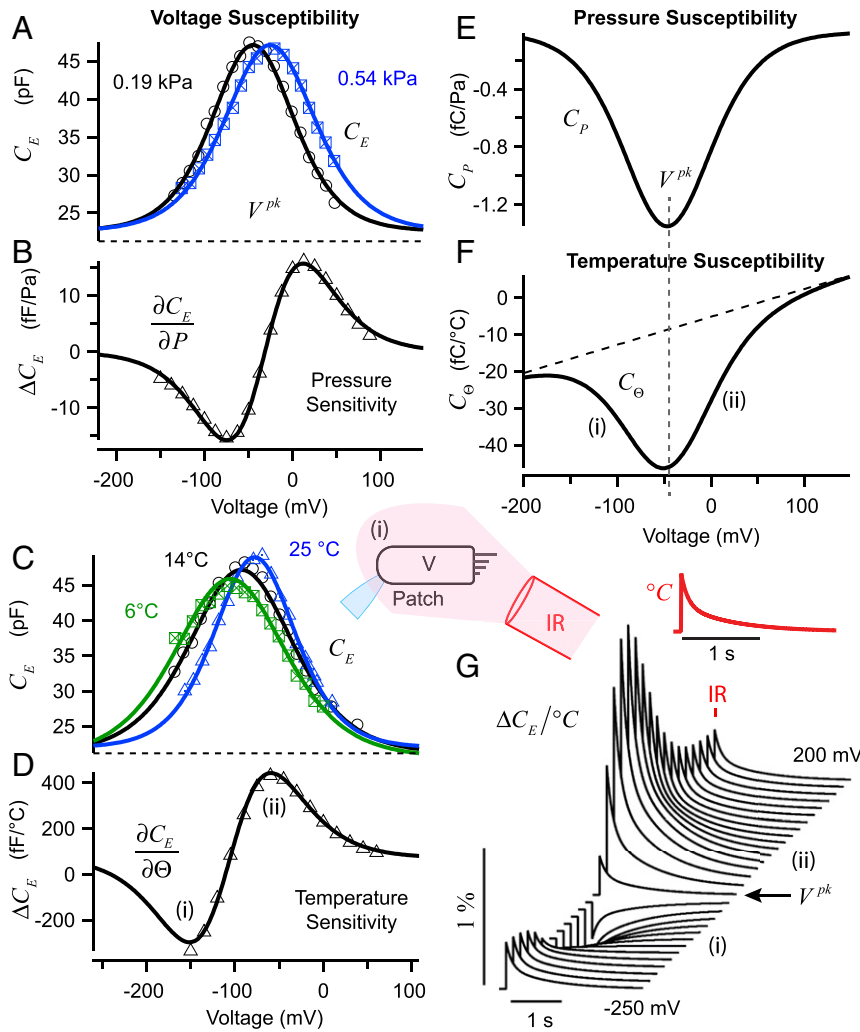
Fig. 1. NLC susceptibility of OHCs. (*A*) Capacitance voltage susceptibility C_E measured at two different intracellular pressures by Kakehata and Santos-Sacchi (21) (symbols) compared to the present piezoelectric theory (solid curves). Nonlinear piezoelectric capacitance is responsible for the bell curve, while the lipid bilayer contributes only a very weak voltage dependence (*SI Appendix*, Fig. S1). (*B*) Change in C_E evoked by a change in pressure. (*C*) Capacitance voltage susceptibility C_E measured at three temperatures by Santos-Sacchi and Huang (22) (symbols) compared to piezoelectric theory (solid curves). (*D*) Change in C_E evoked by a change in temperature. (*E*) Capacitance pressure susceptibility C_P for the OHC in *A*. (*F*) Capacitance temperature susceptibility C_Θ for the OHC in *C* with V^{pk} shifted to resting potential of −47 mV. The bell-shaped curve arises from piezoelectricity while the straight dashed line arises from the lipid bilayer. (*G*) Change in capacitance C_E evoked by an infrared laser heat pulse (*Inset, i*) at different holding potentials (black curves). Results are for a 1 °C increase in temperature occurring in 500 μs followed by relaxation to resting temperature over ~1 s (*Inset*, red) (parameters for all figures are listed in Table 1).

$$C_\Theta = C_\Theta^L + C_E^{pk}\beta_\Theta f(\xi). \qquad [4]$$

To first order, the contribution from the passive membrane is $C_\Theta^L \approx C_E^0 c_1(V + \psi)$, where ψ is the spontaneous polarization arising from the ionic conditions, and c_1 is the "thermostriction" coefficient arising primarily from thinning of the membrane that occurs with increases in temperature. Thermostriction, derived here from thermo-piezoelectricity, is the thermal analog to electrostriction in lipid bilayers (19) and explains the origins of capacitive currents induced by infrared laser pulses in passive membranes (14) (*SI Appendix*, Fig. S2). The contribution from the piezoelectric domains $C_E^{pk}\beta_\Theta f(\xi)$ is closely related to the capacitance voltage susceptibility and is found by taking the partial derivative of the charge displacement with respect to temperature.

Fig. 1*F* plots the capacitance temperature susceptibility C_Θ for OHCs. The dashed line in Fig. 1*F* is the contribution of the passive membrane C_Θ^L, while the solid curve is the total capacitive temperature susceptibility including the contribution of piezoelectricity (Eq. **4**). It is important to note that C_Θ cannot be completely

determined by temperature-dependent changes in electrical capacitance susceptibility alone. This is most clearly illustrated by the fact that C_Θ in Fig. 1*F* is negative for all voltages below the spontaneous polarization and hence the heat-pulse–evoked current is always inward and excitatory. The change in electrical capacitance (Fig. 1*D*), in contrast, reverses sign, which would imply a change in the direction of the capacitive current in models based simply on variable capacitance (15). This distinction is illustrated for an OHC in Fig. 1*G* where ΔC_E is shown as a function of time in response to an infrared (IR) laser pulse raising the temperature 1 °C in 500 μs followed by slow thermal relaxation (inset *i* illustrates IR radiation of the OHC). There is a very strong voltage dependence in the IR-evoked change in electrical capacitance susceptibility that reverses sign with voltage, quantitatively matching experimental results in OHCs and SLC26a5-transfected cells (22, 23).

Speed and Load Dependence of OHC Charge Displacement. The OHC motor residing in the membrane always operates against a mechanical load, arising from the cell itself and the external

Table 1. Parameters

Symbol	Value (SI units)	Description	Present estimation method	Data source
a_2	0.13 (V^{-2})	Electrostriction coefficient	See *SI Appendix*, Fig. S1	Based on refs. 43 and 44
c_1	0.0036 ($°C^{-1} \cdot V^{-1}$)	Thermostriction coefficient	See *SI Appendix*, Fig. S2	Based on ref. 14
C_E^L	Variable (F)	Linear electrical capacitance susceptibility. OHC size dependent (~1 $\mu F \cdot cm^{-2}$)	Curve fit Eq. **2** to low-frequency NLC data (Fig. 1A)	E.g., refs. 21, 45, and 46
C_E^{pk}	Variable (F)	Peak piezoelectric electrical capacitance susceptibility. Prestin expression dependent (nominal 1.1 C_E^L)	Curve fit Eq. **2** to low-frequency NLC data (Fig. 1A)	E.g., refs. 21 and 46
l_c	Variable (m)	Hair cell length. Cochlear place dependent	Set by cochlear place	*SI Appendix* and Fig. 3A, based on ref. 41
n patch, macropatch, and cochlea	0.7 (–)	Fractional derivative governing relaxation spectrum	From power law frequency roll-off of the real NLC	Data from Fig. 2 and ref. 24
n μ-chamber	0.8 (–)	Fractional derivative governing relaxation spectrum	Curve fit frequency dependence of cell displacement	Data from Fig. 2 and ref. 2
V^{pk}	−0.047 (V)	Voltage of peak NLC	Curve fit Eq. **2** to low-frequency NLC data (Fig. 1A)	E.g., refs. 21 and 46
β_P	−0.054 ($V^{-1} \cdot kPa^{-1}$)	Pressure sensitivity	Curve fit Eqs. **2** and **3** to low-frequency NLC data (Fig. 1 A and B)	Data from ref. 21
β_Θ	−0.0012 ($V^{-1°} \cdot C^{-1}$)	Temperature sensitivity	Curve fit Eqs. **2** and **4** to the low-frequency NLC (Fig. 1 C and D)	Data from ref. 22
$\delta^c f$ μ-chamber	−0.118 (V^{-1})	Effective OHC piezoelectric strain coefficient times f in microchamber experiments	Fit Eq. **5**, with $0 < f < 1$ treated as unknown, and compliance known (Fig. 2B)	Data from Fig. 4 and in ref. 2
δ^c patch and cochlea	−0.412 (V^{-1})	Whole-cell OHC piezoelectric strain coefficient at V^{pk} (note: $\delta^c \approx \delta^p \varphi f$)	Fit Eq. **5**. to low-frequency OHC strain under zero load	Based on refs. 47 and 48
κ^c	3.5×10^6 (N^{-1})	Low-frequency OHC compliance, strain per Newton at V_{pk}	Low-frequency whole-cell compliance converted to strain per Newton	Based on refs. 2 and 49
$(\kappa^c + \kappa^L)/\kappa^L$ isolated cell	1 (–)	External load compliance $\kappa^L \to \infty$ for an isolated cell	By definition	
$(\kappa^c + \kappa^L)/\kappa^L$ cochlea	2 (–)	Load compliance κ^L in the cochlea comes from the internal OHC stiffness and the external load stiffness	Stiffnesses matched	Based on power efficiency, e.g., ref. 30
$\kappa^p \varphi/\kappa^c$	0.8 (–)	Ratio of compliance of the piezoelectric domain $\kappa^p \varphi$ to the whole-cell κ^c	From frequency roll-off of real NLC and magnitude of the imaginary NLC relative to the real NLC	Based on refs. 13 and 27
λ	0.032 (V)	Voltage sensitivity	Curve fit Eq. **2** to low-frequency NLC data (Fig. 1A)	Data from refs. 21 and 46
τ^p	2×10^{-7} (s)	Relaxation time constant of piezoelectric domain	Lack of corner in Bode force up to 80 kHz	Based on Fig. 4 from ref. 2
τ^c	2×10^{-7} (s)	Relaxation time constant of composite	Lack of corner in Bode force up to 80 kHz	Based on Fig. 4 from ref. 2
τ_{RC}	Variable (s)	Electrical time constant of the OHC. OHC size and location dependent	From cochlear map	*SI Appendix* and Fig. 3B, based on refs. 9 and 42
ω_n isolated cell	ω_{iN} variable (s^{-1})	Natural frequency of the isolated OHC based on cell length	Frequency where OHC disp. phase is $-\pi/2$ μ-chamber	*SI Appendix* and Fig. 3C, based on Fig. 2 from ref. 2
ω_n cochlea	Variable (s^{-1})	Natural frequency of the cochlear load at the tonotopic place	Defined by cochlear place principle	*SI Appendix* and Fig. 3 A and B abscissa, refs. 41 and 42
ω_ζ isolated cell	$\omega_n/2$ (s^{-1})	Viscous corner frequency of the OHC in media based on cell size. (damping coefficient $\zeta \approx 1$)	Curve fit Bode plots in μ-chamber configuration	From Fig. 2 and ref. 2
ω_ζ cochlea	$1.4\omega_n$ (s^{-1})	Damping corner frequency of the combined OHC and cochlear load. (damping coefficient $\zeta \approx 0.36$)	Underdamped based on passive cochlear tuning	E.g., refs. 50 and 51

environment. As a result, OHCs invoke capacitance voltage susceptibility and stress susceptibility at the same time, with the combination of the two providing the total electrical charge displacement and mechanical strain in the membrane. To examine how the load influences OHC function high frequencies, constitutive equations for the passive membrane and the piezoelectric domains were combined as a mixture composite and subjected to a mechanical load imposed by the cell itself and the external environment. Equations were simplified for small perturbations in voltage and axial force, and converted to the frequency domain (*Methods* and *SI Appendix*, A and B).

To examine intrinsic speed of the motor element, the cell was clamped to a fixed length (strain = 0) and excited by sinusoidal voltage clamp. Although the whole-cell strain was zero in the simulations, the

motor domain was allowed to extend into the passive domain based on their respective viscoelastic properties (Fig. 2*A* and *SI Appendix*, Eqs. **B1**–**B5**). The force $\tilde{B}$ required to prevent the OHC from changing length in response to voltage $\tilde{V}$ is (tildes denote the frequency domain):

$$F_V(\omega) = \frac{\tilde{B}}{\tilde{V}} = -\frac{\tilde{\delta}^c}{\tilde{\kappa}^c}, \qquad [5]$$

where the composite piezoelectric coefficient is $\tilde{\delta}^c = \delta^c f(\xi)/(1 + j\omega\tau^p)$ and the composite compliance is $\tilde{\kappa}^c = \kappa^c/(1 + j\omega\tau^c)$. The material parameter and δ^c is the composite piezoelectric strain coefficient at $\xi = 0$ ($f(\xi) = 1$). Time constants τ^p and τ^c govern the intrinsic speed(s) of piezoelectric strain extension into the passive domain under zero whole-cell strain. Elegant experiments by Frank et al. (2) measured $F_V(\omega)$ by inserting the basal pole of OHCs into a large pipette (μ-chamber) to control the extracellular voltage acting on the basal region of the cell, and measuring the force generated in the frequency domain using an atomic-force microscope. Experiments were conducted under nearly constant cell length, with results revealing a flat gain and phase of $F_V(\omega)$ relative to the μ-chamber voltage up to at least 80 kHz. The measured force did not depend on the length of the cell extending outside of the μ-chamber, consistent with Eq. 5. Although the precise intracellular voltage was not known in the Frank et al. experiments [i.e., $f(\xi)$ and transmembrane V not known], a very broad frequency response was clearly demonstrated. The Frank et al. force data are compared to the present model in Fig. 2*B*. Simulations required a reduced piezoelectric coefficient $\tilde{\delta}$ relative to voltage-clamp conditions to account for the difference in voltage and f in the μ-chamber configuration (Table 1). The relatively flat gain and phase (Fig. 2*B*) requires the time constants governing intrinsic speed of the motor to be less than ~3 μs in OHCs. This means the instantaneous coulomb force acting on the piezoelectric charge (voltage sensor) is transferred to the whole cell in less than 3 μs. These results show the isometric force generation is ultrafast, with changes in isometric force capable of tracking the electric field cycle-by-cycle at all physiologically relevant frequencies. The situation is quite different if the cell is allowed to change length. The coulomb force is still instantaneous when the cell is allowed to deform, but it takes time for cell to displace as the force drives against the viscosity and mass of the load.

The whole-cell displacement was examined to determine how the viscoelastic properties of the external load and the OHC itself limit speed of electromotility. The displacement $\tilde{D}$ in response to sinusoidal voltage clamp is as follows:

$$D_V = \frac{\tilde{D}}{\tilde{V}} = \frac{l_c \tilde{\delta}_c}{H_L}, \qquad [6]$$

where l_c is the length of cell and H_L is the nondimensional mechanical impedance of the total mechanical load. Three specific loads were considered: 1) OHC in isolation where H_L arises from intrinsic properties of the cell itself plus the fluid media, 2) a membrane patch where H_L arises from intrinsic properties of the patch and fluid, and 3) OHC in the cochlea where H_L arises from the cell plus the extracellular cochlear load. In all three cases, the load was modeled as a spring-mass-damper system. Specifically, $H_L = ((\tilde{\kappa}^c + \tilde{\kappa}^L)/\tilde{\kappa}^L)(1 - (\omega/\omega_n)^2 + j^n(\omega/\omega_\zeta)^n)$, where $(\tilde{\kappa}^c + \tilde{\kappa}^L)/\tilde{\kappa}^L$ is the ratio of the total compliance divided by compliance of the load, ω_n is the undamped natural frequency of the load, and ω_ζ is the damping corner frequency (nondimensional damping coefficient $\zeta \approx \omega_n/2\omega_\zeta$ for $n = 1$). The fractional derivative n models the relaxation spectrum arising from the frequency-dependent viscous properties (*SI Appendix*, Eq. **B5**).
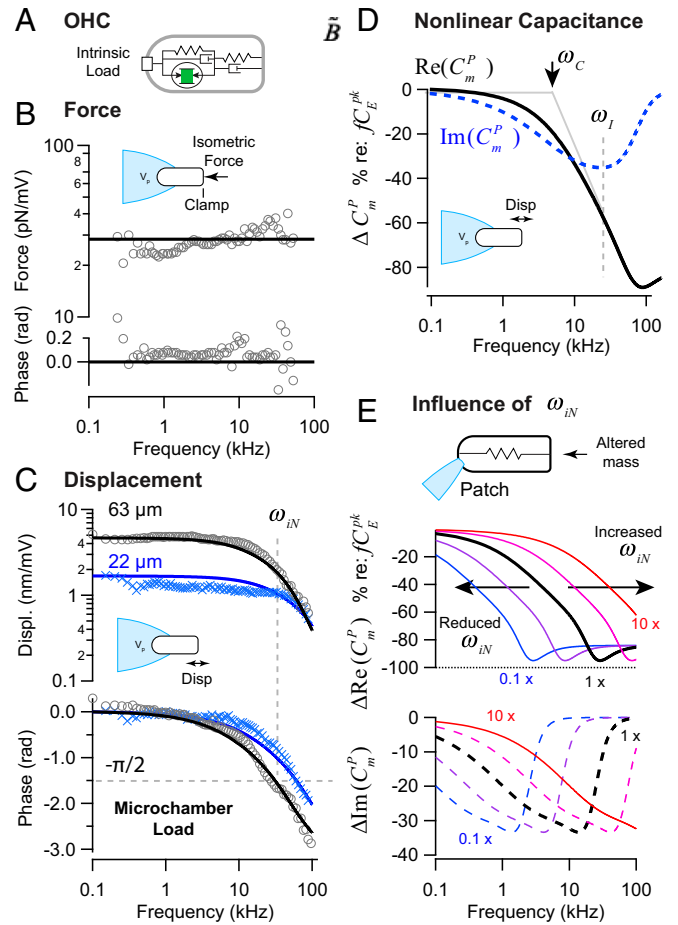

Fig. 2. Speed of OHC force and electromotility. (*A*) Schematic of an OHC subject to intrinsic load arising from viscoelasticity and the fluid media. (*B*) Force generated by controlling the voltage using an extracellular μ-chamber enveloping the base of an OHC reported by Frank et al. (2) (symbols) compared to piezoelectric theory linearized about a holding potential (black curves). (*C*) Voltage-evoked OHC displacement reported by Frank et al. (symbols) compared to piezoelectric theory for two cell lengths extending beyond the μ-chamber (black, blue). The intrinsic natural frequency of the extended portion of the cell is ω_{iN}, which occurs when the load is dominated by viscous drag and the phase is $-\pi/2$ radians. (*D*) Change in the real NLC [black, $Re(\bar{C}_m^p)$] and imaginary NLC [blue, $Im(\bar{C}_m^p)$] as functions of frequency associated with the black curve in C (relative to the peak as $\omega \to 0$). The real part of the NLC rolls off at corner frequency ω_c as the viscous load begins to draw power from the piezoelectric charge displacement. The imaginary NLC (dashed) is tuned to a specific frequency ω_I, which is near the frequency of peak piezoelectric power output in the unloaded μ-chamber configuration. (*E*) For an unloaded cell, the imaginary NLC and piezoelectric power output to the viscous load is tuned to the intrinsic natural frequency of the cell itself ω_{iN} (shown in whole-cell voltage-clamp configuration).

Parameters are provided in Table 1 for all loading conditions. For an isolated OHC, the stiffness arises from the cell itself [$(\tilde{\kappa}^c + \tilde{\kappa}^L)/\tilde{\kappa}^L = 1$, $\tilde{\kappa}^L \to \infty$], while mass and viscosity arise from the OHC plus the extracellular media. Due to the high viscosity and low mass, isolated OHCs do not show resonance or tuning in their displacement evoked by voltage. Lack of displacement tuning is demonstrated in Fig. 2*C*, which shows OHC voltage-evoked displacement data from Frank et al. (2) in the μ-chamber configuration. Like Fig. 2*B*, the precise amplitude of the transmembrane voltage was not measured in the experiments, but the frequency response is still revealing. Experimental data (symbols) are compared to Eq. 6 (solid curves) for two different cell lengths extending outside the μ-chamber. Model parameters (Table 1) are the same

for all curves in Fig. 2 *A–D*, with the exception of length outside the chamber in Fig. 2*C* (black, blue). Although the force generated under zero strain is independent of frequency (Fig. 2*B*), the displacement under zero force begins to roll off as the frequency is increased (Fig. 2*C*). The roll-off arises from intrinsic viscosity and mass of the cell. The frequency with a displacement phase of $-\pi/2$ defines the intrinsic natural frequency ω_{iN} of the unloaded cell (Fig. 2*C*, vertical dashed line) where mass and stiffness cancel and OHC power output is dissipated by the intrinsic viscous load (see *SI Appendix* and Fig. 3 for isolated OHC ω_n based on cell length). Although the displacement shows no frequency tuning, the power output to the viscous load does.

Electromechanical behavior of the OHC, including power output, can be determined from whole-cell capacitance recordings. When the OHC is under load, charge displacement arises from both the capacitance voltage susceptibility and the capacitance stress susceptibility. Under voltage-clamp conditions in the frequency domain, the two terms provide the total electrical displacement current as $\tilde{I_D} = j\omega \tilde{C}_m^p \tilde{V}$, where the complex-valued NLC is as follows (*SI Appendix*, Eq. **B6**):

$$\tilde{C}_m^p = C_E^{pk} f(\xi) H_C,$$ [7a]

$$H_C = 1 - \frac{\tilde{\kappa}^p \varphi}{\tilde{\kappa}^c}\left(\frac{H_L - 1}{H_L}\right).$$ [7b]

$\tilde{C}_m^p$ is the complex-valued analog to the real-valued NLC commonly discussed in the literature for OHCs. For consistency with earlier reports, $Re(\tilde{C}_m^p)$ is termed the real NLC (Re NLC), and $Im(\tilde{C}_m^p)$ is termed the imaginary NLC (Im NLC). Nonlinearity appears through $f(\xi)$, while load dependence arises from H_L. The nondimensional ratio $\tilde{\kappa}^p \varphi / \tilde{\kappa}^c$ in Eq. **7** plays an important role and is the compliance of the piezoelectric domain divided by the compliance of the whole cell. If the piezoelectric domain had zero compliance, it would not deform under load and Eq. **7** would predict zero frequency dependence of Re NLC, which is known not to be the case (13). The fact that $\tilde{C}_m^p$ is frequency dependent means the piezoelectric domain is compliant, and the magnitude of compliance can be estimated from the frequency dependence of NLC.

The NLC described by Eq. **7** is reversible and no net charge is lost, yet the piezoelectric capacitance has an imaginary component that leads to what would be interpreted experimentally as an electrical conduction current. Frequency-domain measurements of whole-cell admittance include a load-dependent effect of piezoelectric charge displacement in both the real and imaginary components. Ignoring this effect can lead to incorrect conclusions about OHC function on the basis of admittance measurements.

The conventional NLC measured experimentally corresponds to the real part of the complex-valued capacitance in Eq. **7** $Re(\tilde{C}_m^p)$, which is the solid black curve in Fig. 2*D* for an OHC in the μ-chamber configuration (Fig. 2*C*, black). The imaginary part $Im(\tilde{C}_m^p)$ for the same cell is the blue dashed curve. Three major conclusions can be drawn from Eq. **7** and results in Fig. 2*D*. First, $Re(\tilde{C}_m^p)$ begins to roll off at a corner frequency ω_c, which in the μ-chamber experiments is aligned with roll-off in whole-cell cell displacement (Fig. 2 *C* and *D*). Second, the roll-off simply reflects the intrinsic load imposed by the media and the cell itself and does not occur if the cell is held at zero strain (Fig. 2*B*). Third, $Im(\tilde{C}_m^p)$ becomes negative as frequency is increased, and peaks at a frequency well above the capacitive corner frequency $\omega_I >> \omega_c$. In isolated cells, the frequency ω_I arises from the intrinsic natural frequency ω_{iN} of the cell itself (Fig. 2*C*). The influence of artificially changing the intrinsic natural frequency of the cell itself is illustrated in Fig. 2*E*. The frequency shift arises from the intrinsic load H_L in Eq. **7**—the load shifts the corner frequency, but does not reflect the intrinsic speed of the motor element itself.
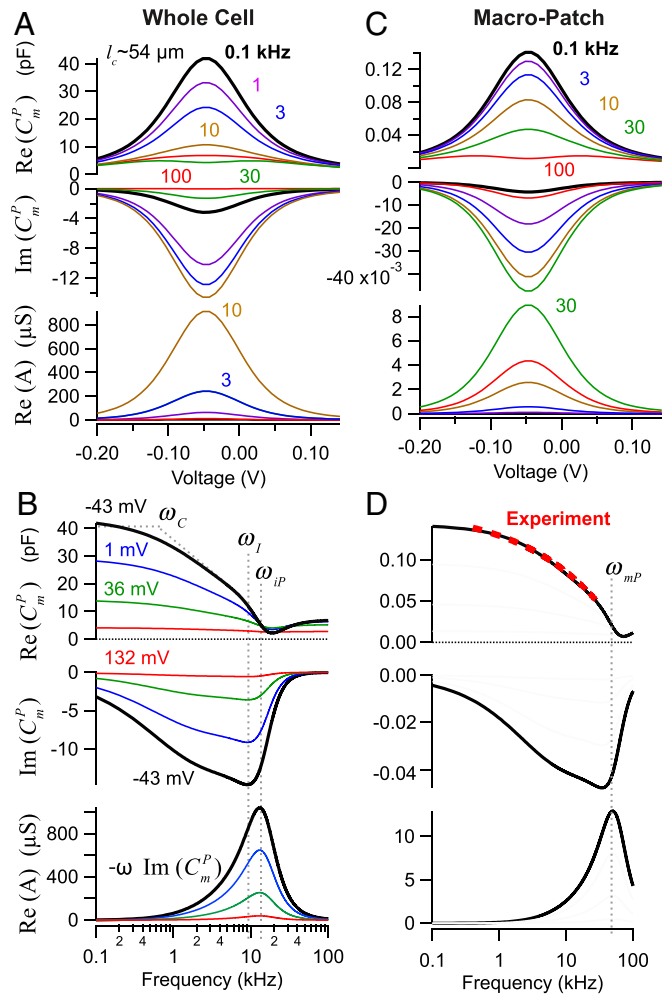

Fig. 3. NLC and power output of an isolated OHC and membrane macropatch. (*A*) NLC of a 54-μm-long OHC in ideal whole-cell voltage clamp at six different frequencies showing a reduction in real NLC [$Re(\tilde{C}_m^p)$] and commensurate increases in imaginary NLC [$Im(\tilde{C}_m^p)$ and real admittance] as the frequency is increased from 0.1 to 10 kHz. (*B*) Frequency dependence of NLC at four different voltages showing a corner frequency ω_c where the real NLC begins to roll off, a much higher frequency ω_I where the imaginary NLC peaks, and an even higher frequency ω_{iP} where the power output and real-valued admittance peaks. The real NLC corner frequency underestimates the best operating frequency by more than an order of magnitude. For isolated OHCs, the power output at frequency ω_{iP} is dissipated by heat, and therefore OHCs in the cochlea must operate at a frequency below the intrinsic ω_{iP}. (*C* and *D*) Isolated membrane patches are predicted to behave similar to whole cells under ideal voltage clamp, with NLC magnitude reduced and intrinsic natural frequency increased according to patch size. The real NLC predicted by the present theory (solid black) overlies macropatch experimental recordings of Santos-Sacchi and Tan (red, dashed) (24). The power law frequency dependence of the real NLC arises in the theory from the broad relaxation spectrum of the viscoelastic membrane (fractional derivative *n* = 0.7). The imaginary NLC is small in macropatch experiments (~40 fF), but when multiplied by frequency results in significant power output (Eq. **8**) peaking at a frequency more than an order of magnitude higher than the real NLC corner frequency.

The imaginary NLC is key to OHC function because it is directly related to the real power output by the following:

$$PWR = \frac{-1}{2}\omega\, Im\left(\tilde{C}_m^p\right)\tilde{V}^2.$$ [8]

Appearance of frequency ω in Eq. **8** pushes the maximum power output frequency even higher, above the peak $Im(\tilde{C}_m^p)$ frequency

ω_I. The peak power output always occurs at a frequency well above the conventional $Re(\tilde{C}_m^p)$ corner frequency ω_c and corresponds to the frequency ω_P when the piezoelectric part of the electrical admittance is peak.

Complex-valued capacitance and frequency-dependent power output are illustrated in Fig. 3 for two voltage-clamp recording conditions: ideal whole-cell voltage clamp of a 54-μm-length OHC (Fig. 3 *A* and *B*), and ideal voltage clamp of an excised membrane macropatch (Fig. 3 *C* and *D*). Fig. 3*A* shows the real and imaginary components of the NLC and real admittance as functions of whole-cell holding potential for six different frequencies (0.1 to 100 kHz), while Fig. 3*B* shows the NLC and admittance as functions of frequency at four different voltages. Results are for an isolated cell subject to intrinsic mass, stiffness, and viscosity arising from the cell itself and the fluid media load. The magnitude of $Re(\tilde{C}_m^p)$ begins rolling off immediately with frequency, while the magnitude of $Im(\tilde{C}_m^p)$ builds up (with no change in voltage dependence if n is held constant with voltage). Frequency dependence under whole-cell voltage clamp is most clearly shown in Fig. 3*B*. Of course, current voltage-clamp technology has a limited frequency bandwidth, but it is still useful to examine what would be expected based on Eqs. **7** and **8** for an isolated cell. The key point is that the imaginary NLC builds up reaching a peak negative value at a frequency ω_I. The maximum power output is determined by the real part of the piezoelectric admittance (bottom panel) and peaks at frequency $\omega_P >> \omega_c$. This occurs because $Re(\tilde{C}_m^p)$ reflects the piezoelectric charge displacement working against reversible elasticity of the cell and the load, while $Im(\tilde{C}_m^p)$ reflects the piezoelectric charge displacement working against the dissipative viscous load.

The NLC of an excised macropatch of membrane (Fig. 3 *C* and *D*) is predicted to follow trends similar to the whole cell (Fig. 3 *A* and *B*), but reduced in magnitude and shifted in frequency because of size and mechanical constraints on the patch. Results in Fig. 3*D* are the most revealing, and directly compare experimental real NLC from Santos-Sacchi and Tan (red dashed curve) (24) to Eq. **7**. $Re(\tilde{C}_m^p)$ measured experimentally exhibits a power-law frequency dependence (red dashed), captured in the model by the broad relaxation spectrum (fractional derivative $n = 0.7$). The imaginary component was not reported, but present results suggest $Im(\tilde{C}_m^p)$ peaks near 30 kHz at −40 fF. Most importantly, peak power output is predicted to occur near 50 kHz in the macropatch configuration, a frequency where the real NLC is almost zero. Hence, the corner frequency of $Re(\tilde{C}_m^p)$ underestimates the best power output frequency ω_P by more than an order of magnitude both in the whole-cell and macropatch configurations. Simulations in Fig. 3 assumed the patch did not induce static stress (i.e., $f(\xi) = 1$) and the relaxation spectrum was constant ($n = 0.7$).

To explore how OHCs function in the cochlea, cells were loaded with a spring-mass-damper system to simulate the tonotopic cochlear load. The natural frequency of the loaded system and the length of the cell were set by a model tonotopic map with (Table 1 and *SI Appendix*, Fig. S3). The complex-valued NLC for a 30-μm OHC under the idealized cochlear load are shown in Fig. 4 *A* and *B* using the same format as Fig. 3. The effect of the cochlear load is to align the best power output frequency of the OHC to the tonotopic place of 2.5 kHz, a frequency well below the intrinsic natural frequency ω_{iN} of the 30-μm-long cell. Results demonstrate capacitance voltage and capacitance stress susceptibility both play a role, providing a feedback mechanism that tunes the real power output of OHCs based on the properties of the load. As noted in *Discussion*, the ability of OHCs to sense and react to the load might be an important factor contributing to the correlation between OHC length and tonotopic location in the cochlea.

Power output of a 30-μm OHC under simulated cochlear load is shown in Fig. 4*C* for an ideal 1-mV voltage-clamp command

(blue) and a low-pass-filtered voltage command (black). Results predict OHC power output is tuned to a narrow frequency band even though isolated OHCs show no tuning in $Re(\tilde{C}_m^p)$ under patch-clamp conditions in the dish (e.g., Fig. 3*B*). The peak power output for the OHC in Fig. 4*C* would be ~10 fW for a 5-mV voltage modulation, similar to the estimate by Wang et al. (25) for OHCs under physiological load in the cochlea. Power output for a 1-mV voltage modulation per $\sqrt{\text{Hz}}$ is shown in Fig. 4*D* for OHCs of five different lengths corresponding to five different locations in the cochlea. Results in Fig. 4*D* are for individual OHCs under low-pass-filtered voltage-clamp conditions, yet the tuning curves show similarity to traveling waves in the cochlea. OHC length, linear capacitance, and membrane conductance were set by the specific location in the cochlea (9, 26) with the voltage rolling off above a passive RC corner in the
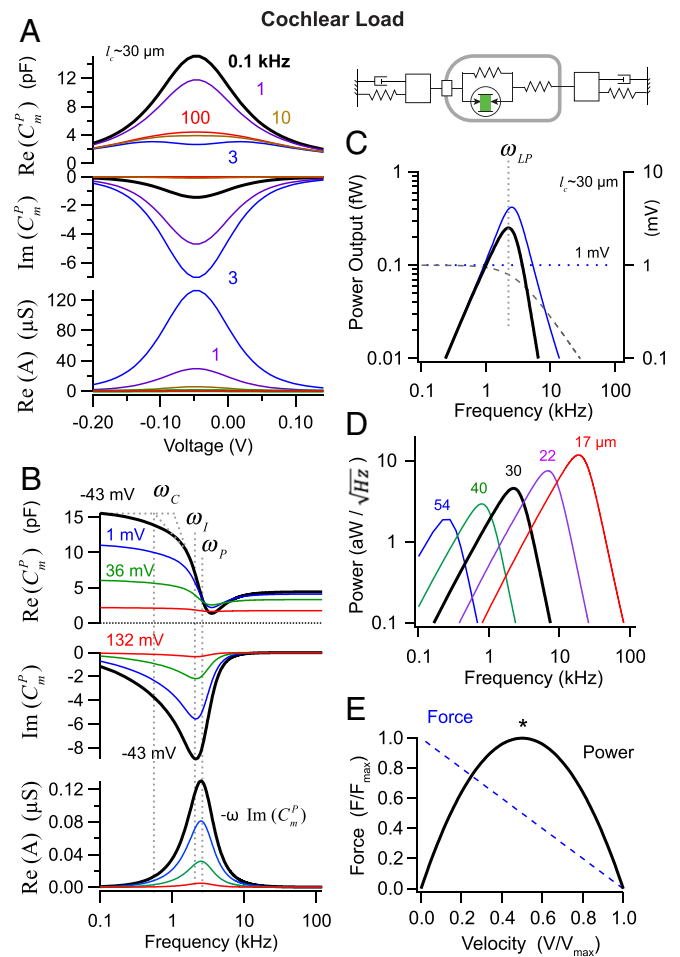

Fig. 4. NLC and power output of OHCs in the cochlea. (*A* and *B*) Real and imaginary parts of the NLC of a 30-μm-long hair cell under simulated load in the cochlea (same format as Fig. 3 for isolated cells and membrane patches). When subject to the cochlear load, the frequency of peak imaginary capacitance is determined by the tonotopic place principle rather than intrinsic mass and stiffness of the cell itself, which requires the OHC to be sufficiently short to allow useful power output at its specific location in the cochlea. (*C* and *D*) Power delivered to the cochlear load based on cell size and tonotopic location under voltage-clamp conditions. (*C*) Power output of a 30-μm-long OHC located at the 2.5-kHz location subject to an underdamped cochlear load as a function of frequency (1-mV voltage-clamp command, blue; 1-mV low-pass-filtered command, black). (*D*) Power output per $\sqrt{\text{Hz}}$ in response to 1-mV low-pass-filtered voltage command for OHCs of different lengths. (*E*) Schematic illustrating peak power output (*) occurs at a load between the isometric force (zero strain) condition and the maximum velocity (zero force) condition.

simulations (e.g., Fig. 4*C*, black dashed). Power output shown in Fig. 4*D* supports the hypothesis that individual OHCs contribute power to cochlear amplification primarily at frequencies near their location in the tonotopic cochlea.

Discussion

The present report is focused primarily on resolving the OHC speed paradox, a paradox most clearly exemplified by disparity between the ultrafast cycle-by-cycle isometric force generated by OHCs (2) vs. the slow low-pass-filtered characteristics of electrical charge displacement in OHC membranes (13). The paradox is resolved using first principles to show how the piezoelectric behavior of OHCs explains both results. High-frequency experimental results of Frank et al. (2) are reproduced in Fig. 2 *A* and *B*, and low-frequency roll-off of NLC reported by Santos-Sacchi and Tan (13) are reproduced in Fig. 3*D* using exactly the same physics. Three major factors were taken into account to resolve the paradox and describe how OHCs function at high frequencies.

The first factor involves interpretation of OHC NLC. The problem with the traditional approach in OHCs is that voltage induces load-dependent stress and strain, and the strain alters the charge displacement. Therefore, the capacitance recorded using conventional methods changes with conditions of the experiment. To describe the charge displacement in the frequency domain requires a load-dependent complex-valued NLC $\tilde{C}_m^p$ (Eq. **7**). The traditional approach is adequate for low frequencies where the coulomb force is resisted by an elastic load, but fails when the force is resisted by viscous or inertial loads, which is always the case at high auditory frequencies. Viscous drag shifts the phase by $-90°$ and introduces a negative-valued imaginary NLC $Im(\tilde{C}_m^p)$, which appears in electrical admittance measurements as a frequency- and voltage-dependent, positive, real-valued admittance. $Im(\tilde{C}_m^p)$ reflects a reversible charge displacement but, as described previously, can be incorrectly interpreted as a conduction current based on traditional interpretation of electrical admittance (27).

The second factor involves the relationship between charge displacement and power output of the OHC. In the frequency domain, the imaginary NLC times frequency $-\omega Im(\tilde{C}_m^p)$ is proportional to the power delivered to mechanical load (Eq. **9**). If $Im(\tilde{C}_m^p) = 0$, the OHC power output is zero. Although the real component of NLC $Re(\tilde{C}_m^p)$ is revealing because it reflects a component of charge displacement, it is not a measure of power output or function of the OHC as a motor. The OHC peak power output frequency ω_P arising from the imaginary NLC is above the corner frequency of the real NLC by more than an order of magnitude, demonstrating why ω_c is a poor indicator of the frequency response or speed of OHCs. Given the thermodynamic origin of complex-valued NLC, this finding likely applies to all conditions: isolated OHCs, membrane patches, and OHCs in the cochlea (Figs. 3 and 4).

The third factor involves how OHCs are loaded in the cochlea vs. loaded in experiments. Experiments in the dish, especially at low frequencies, often result in very small $Im(\tilde{C}_m^p)$ because the OHC is working against an elastic load that does not absorb significant power. In the cochlea, OHCs work against a mechanical load consisting of elasticity, viscosity, and mass. Each location along the tonotopic map has a characteristic best frequency where the elastic force nearly balances the inertial force and the load becomes dominated by viscous drag. Present results indicate OHC power output is just before the traveling wave peak (28), with OHCs basal to the peak contributing to amplification (29) but at lower levels (Fig. 3*E*).

For efficient operation in the cochlea, OHCs must be sufficiently short to operate below their own intrinsic natural frequency, but sufficiently long to generate the required velocity. The relationship between power output and velocity (for frequencies near ω_P) is illustrated schematically in Fig. 4*D* as the load

changes from high drag (zero velocity, maximum force) to low drag (maximum velocity, zero force). Similar to skeletal muscle (30), OHC power output is maximized between the two extreme loading conditions. These two factors likely combine with electrical factors and channel expression to determine optimum OHC length as a function of best frequency in the cochlea.

The present report demonstrates how OHCs deliver cycle-by-cycle power to the cochlear amplifier at high frequencies well above the corner frequency defined by the real NLC. The analysis is agnostic to the specific molecules responsible for piezoelectricity but places constraints on what is thermodynamically feasible. It is known that OHC electromotility requires expression of the transmembrane protein *prestin*, a member of the SLC26 family of anion transporters (3, 31, 32). There is strong evidence that Cl^- is essential and is electrostatically bound in the central core region of the protein (33–35). In the absence of Cl^-, piezoelectric NLC is lost in OHCs but can be restored by inserting a charged residue near the putative Cl^- binding site in the core domain (36). These data support the hypothesis that the charge responsible for the piezoelectric coulomb force in *wt* OHCs is likely to be electrostatically bound Cl^- located in the prestin core. A force-driven conformational change in prestin could underlie piezoelectric behavior, but the present analysis is thermodynamic in nature and cannot distinguish between molecular mechanisms involving a single transition, "N" intermediate transition states, continuous transitions, or other hypothetical mechanisms that may involve interplay between charge, lipid, and protein. Differences on the molecular scale are subtle on the thermodynamic scale. For example, replacing the high-dimensional Langevin nonlinearity f with a two-state Boltzmann function (37) or a multistate model (20) introduces a small change in the shape of the nonlinear voltage distribution but does not change any conclusions of the present report. The direct coupling between piezoelectric charge displacement and strain in OHCs (6) contrasts voltage-gated ion channels where the gating charge displacement precedes conformational changes responsible for channel open probability (38). Hence, the term charge displacement is used here to avoid confusion with the term gating charge, which is traditionally associated with displacement of specific residues preceding a protein-scale conformational change. The present analysis further implies the piezoelectric coulomb force is always present within the membrane electric field, and that voltage-dependence arises from the saturating compliance of the piezoelectric element rather than charge shielding or charge movement outside the electric field (*SI Appendix*, Eqs. **A5**–**A7**). Consistent with this, force generation is ultrafast, reflecting the instantaneous coulomb force, while the speed of charge displacement is slower reflecting the speed of deformation against the intrinsic and external loads.

The present analysis uses a simple piezoelectric model to demonstrate the importance of the load on OHC motor function, how the complex-valued NLC is related to power output by the cell, and why OHC power output is highest at frequencies well above the real NLC corner. All results were driven by voltage-clamp commands, which differs from the cochlea where OHCs are driven by MET currents and mechanical forces. Power tuning curves in Fig. 3 *D* and *E* partially account for the OHC electrical corner frequency by driving the cell with a low-pass-filtered voltage, but no attempt was made to address the influence of MET kinetics (39), ion channel gating and expression (9, 10), prestin expression (31), hair bundle electromotility (40), inhomogeneous expression and deformation, or mechanical forces associated with the traveling wave. The present OHC model is minimalistic, and reduces a complex cell with inhomogeneous expression and properties into a single lumped element, yet is sufficient to resolve the OHC speed paradox.

Methods

Electro-mechanical behavior, including capacitance susceptibility, has origins in the Gibbs free energy of the membrane complex. In the present analysis, themo-electromechanical behavior is examined within a control volume encompassing the entire membrane complex (see *SI Appendix* for compete

derivation). The control volume includes the inhomogeneous lipid bilayer, membrane-associated structural proteins, and charged coupled proteins including prestin, but the approach is agnostic to the specific molecular arrangements and mechanisms. Under plane-stress thermodynamic equilibrium conditions, the Gibbs free energy relates small changes in the mechanical stress T_j and strain S_j to small changes in temperature Θ' and transverse electric field (17, 18). Key constitutive parameters are as follows: compliance tensor κ_{ij}, piezoelectric coefficients δ_j, thermal expansion coefficients α_j, electrostriction coefficients γ_j, electrical permittivities ε_j, and pyroelectric coefficients p_j. The OHC membrane was modeled a mixture of a piezoelectric material (p: δ_j^p) occupying area fraction φ and a passive material (s: $\delta_j^s = 0$) occupying area fraction $(1 - \varphi)$. A single time constant for each domain was used to model the speed of deformation under a step change in load. Constitutive parameters for the two materials combine to determine the effective piezoelectric coefficient and compliance of the composite. The general equations were simplified for a thin membrane subject to a transverse electric field. Equations were further simplified to a discrete lumped parameter model assuming axisymmetric, isotropic, isochoric, whole-cell deformations. Model parameters were determined from previously published experimental data primarily from guinea pig OHCs as detailed in Table 1. Model parameters were estimated for the composite membrane, without explicit determination of the area fraction or properties of individual constituents.

To estimate power output under cochlear load, the frequency-dependent load in the cochlea was simulated using a spring-mass-damper system with the natural frequency ω_n corresponding to the place principle in the cochlea. The load was slightly underdamped, $\omega_n = 1.3\omega_\zeta$ rad · s^{-1}. For simulations in Fig. 4 C and D, the OHC size (length, membrane area, linear capacitance) and the passive RC corner frequency (conductance) were set according to a model place principle to illustrate how OHCs of different length deliver power to the cochlear amplifier (*SI Appendix*, Fig. S3). OHC lengths and intrinsic natural frequency are based on the guinea pig frequency map (41), while electrical passive electrical is based on gerbil (9, 42). Frequency domain simulations in the present study were done using identical piezoelectric material parameters at V^{pk} for all OHCs (φ, $\bar{\delta}^c$, and $\bar{\kappa}^c$), changing only length and loading conditions.

Data Availability. All data are from previously published reports as cited in Table 1. Parameter curve fitting and figures were generated using the software Igor64 (WaveMetrics). All study data are included in the article and *SI Appendix*.

1. W. E. Brownell, C. R. Bader, D. Bertrand, Y. de Ribaupierre, Evoked mechanical responses of isolated cochlear outer hair cells. *Science* **227**, 194–196 (1985).
2. G. Frank, W. Hemmert, A. W. Gummer, Limiting dynamics of high-frequency electromechanical transduction of outer hair cells. *Proc. Natl. Acad. Sci. U.S.A.* **96**, 4420–4425 (1999).
3. J. Zheng et al., Prestin is the motor protein of cochlear outer hair cells. *Nature* **405**, 149–155 (2000).
4. J. Curie, P. Curie, Contractions and expansions produced by voltages in hemihedral crystals with inclined faces. *CR (East Lansing Mich.)* **93**, 1137–1140 (1881).
5. J. Ludwig et al., Reciprocal electromechanical properties of rat prestin: The motor molecule from rat outer hair cells. *Proc. Natl. Acad. Sci. U.S.A.* **98**, 4178–4183 (2001).
6. J. Santos-Sacchi, W. Tan, The frequency response of outer hair cell voltage-dependent motility is limited by kinetics of prestin. *J. Neurosci.* **38**, 5495–5506 (2018).
7. A. Vavakou, N. P. Cooper, M. van der Heijden, The frequency limit of outer hair cell motility measured in vivo. *eLife* **8**, e47667 (2019).
8. A. J. Hudspeth, D. P. Corey, Sensitivity, polarity, and conductance change in the response of vertebrate hair cells to controlled mechanical stimuli. *Proc. Natl. Acad. Sci. U.S.A.* **74**, 2407–2411 (1977).
9. S. L. Johnson, M. Beurg, W. Marcotti, R. Fettiplace, Prestin-driven cochlear amplification is not limited by the outer hair cell membrane time constant. *Neuron* **70**, 1143–1154 (2011).
10. M. C. Perez-Flores et al., Cooperativity of Kv7.4 channels confers ultrafast electromechanical sensitivity and emergent properties in cochlear outer hair cells. *Sci. Adv.* **6**, eaba1104 (2020).
11. J. Santos-Sacchi, The speed limit of outer hair cell electromechanical activity. *HNO* **67**, 159–164 (2019).
12. J. Santos-Sacchi, K. H. Iwasa, W. Tan, Outer hair cell electromotility is low-pass filtered relative to the molecular conformational changes that produce nonlinear capacitance. *J. Gen. Physiol.* **151**, 1369–1385 (2019).
13. J. Santos-Sacchi, W. Tan, Complex nonlinear capacitance in outer hair cell macropatches: Effects of membrane tension. *Sci. Rep.* **10**, 6222 (2020).
14. M. G. Shapiro, K. Homma, S. Villarreal, C. P. Richter, F. Bezanilla, Infrared light excites cells by changing their electrical capacitance. *Nat. Commun.* **3**, 736 (2012).
15. M. Plaksin, E. Shapira, E. Kimmel, S. Shoham, Thermal transients excite neurons through universal intramembrane mechanoelectrical effects. *Phys. Rev. X* **8**, 12 (2018).
16. T. Heimburg, The capacitance and electromechanical coupling of lipid membranes close to transitions: The effect of electrostriction. *Biophys. J.* **103**, 918–929 (2012).
17. H. F. Tiersten, Electroelastic equations for electroded thin plates subject to large driving voltages. *J. Appl. Phys.* **74**, 3389–3393 (1993).
18. J. S. Yang, R. C. Batra, A theory of electroded thin thermopiezoelectric plates subject to large driving voltages. *J. Appl. Phys.* **76**, 5411–5417 (1994).
19. R. P. Feynman, *Forces and Stresses in Molecules*, (Massachusetts Institute of Technology, 1939), p. 30.
20. B. Farrell, B. L. Skidmore, V. Rajasekharan, W. E. Brownell, A novel theoretical framework reveals more than one voltage-sensing pathway in the lateral membrane of outer hair cells. *J. Gen. Physiol.* **152**, e201912447 (2020).
21. S. Kakehata, J. Santos-Sacchi, Membrane tension directly shifts voltage dependence of outer hair cell motility and associated gating charge. *Biophys. J.* **68**, 2190–2197 (1995).
22. J. Santos-Sacchi, G. Huang, Temperature dependence of outer hair cell nonlinear capacitance. *Hear. Res.* **116**, 99–106 (1998).
23. O. Okunade, J. Santos-Sacchi, IR laser-induced perturbations of the voltage-dependent solute carrier protein SLC26a5. *Biophys. J.* **105**, 1822–1828 (2013).
24. J. Santos-Sacchi, W. Tan, Voltage does not drive prestin (SLC26a5) electro-mechanical activity at high frequencies where cochlear amplification is best. *iScience* **22**, 392–399 (2019).
25. Y. Wang, C. R. Steele, S. Puria, Cochlear outer-hair-cell power generation and viscous fluid loss. *Sci. Rep.* **6**, 19475 (2016).
26. R. Fettiplace, J. H. Nam, Tonotopy in calcium homeostasis and vulnerability of cochlear hair cells. *Hear. Res.* **376**, 11–21 (2019).

27. B. Farrell, R. Ugrinov, W. Brownell, "Frequency dependence of admittance and conductance of the outer hair cell" in *Auditory Mechanisms, Processes and Models*, A. Nuttall, T. Ren, K. Gillespie, K. Grosh, E. de Boer, Eds. (World Scientific, Singapore, 2006), pp. 231–232.
28. W. Dong, E. S. Olson, Detection of cochlear amplification and its activation. *Biophys. J.* **105**, 1067–1078 (2013).
29. J. A. Fisher, F. Nin, T. Reichenbach, R. C. Uthaiah, A. J. Hudspeth, The spatial pattern of cochlear amplification. *Neuron* **76**, 989–997 (2012).
30. A. F. Huxley, Muscular contraction. *J. Physiol.* **243**, 1–43 (1974).
31. M. L. Seymour et al., Membrane prestin expression correlates with the magnitude of prestin-associated charge movement. *Hear. Res.* **339**, 50–59 (2016).
32. J. Ashmore, Outer hair cells and electromotility. *Cold Spring Harb. Perspect. Med.* **9**, a033522 (2019).
33. D. Oliver et al., Intracellular anions as the voltage sensor of prestin, the outer hair cell motor protein. *Science* **292**, 2340–2343 (2001).
34. D. Oliver, T. Schachinger, B. Fakler, Interaction of prestin (SLC26A5) with monovalent intracellular anions. *Novartis Found Symp.* **273**, 244–253, NaN–260, 261–264 (2006).
35. J. D. Walter, M. Sawicka, R. Dutzler, Cryo-EM structures and functional characterization of murine Slc26a9 reveal mechanism of uncoupled chloride transport. *eLife* **8**, e46986 (2019).
36. D. Lenz, J. Hartmann, D. Oliver, "Local electrostatics control electromotile conformational transitions of Prestin/SLC26A5" in *Proceedings of the 43rd Annual Meeting of the* Association for Research in Otolaryngology (Association for Research in Otolaryngology, 2020), PS 996.
37. K. H. Iwasa, A two-state piezoelectric model for outer hair cell motility. *Biophys. J.* **81**, 2495–2506 (2001).
38. C. M. Armstrong, F. Bezanilla, Currents related to movement of the gating particles of the sodium channels. *Nature* **242**, 459–461 (1973).
39. A. W. Peng, R. Gnanasambandam, F. Sachs, A. J. Ricci, Adaptation independent modulation of auditory hair cell mechanotransduction channel open probability implicates a role for the lipid bilayer. *J. Neurosci.* **36**, 2945–2956 (2016).
40. D. Ó Maoiléidigh, A. J. Hudspeth, Effects of cochlear loading on the motility of active outer hair cells. *Proc. Natl. Acad. Sci. U.S.A.* **110**, 5474–5479 (2013).
41. R. Pujol, M. Lenoir, S. Ladrech, F. Tribillac, G. Rebillard, "Correlation between the length of outer hair cells and the frequency coding of the Cochlea" in *Auditory Physiology and Perception*, Y. Cazals, K. Horner, L. Demany, Eds. (Pergamon, 1992), pp. 45–52.
42. M. Müller, The cochlear place-frequency map of the adult and developing Mongolian gerbil. *Hear. Res.* **94**, 148–156 (1996).
43. O. Alvarez, R. Latorre, Voltage-dependent capacitance in lipid bilayers made from monolayers. *Biophys. J.* **21**, 1–17 (1978).
44. B. Farrell, C. Do Shope, W. E. Brownell, Voltage-dependent capacitance of human embryonic kidney cells. *Phys. Rev. E Stat. Nonlin. Soft Matter Phys.* **73**, 041930 (2006).
45. K. H. Iwasa, Effect of stress on the membrane capacitance of the auditory outer hair cell. *Biophys. J.* **65**, 492–498 (1993).
46. J. Santos-Sacchi, S. Kakehata, S. Takahashi, Effects of membrane potential on the voltage dependence of motility-related charge in outer hair cells of the guinea-pig. *J. Physiol.* **510**, 225–235 (1998).
47. J. F. Ashmore, A fast motile response in guinea-pig outer hair cells: The cellular basis of the cochlear amplifier. *J. Physiol.* **388**, 323–347 (1987).
48. J. Santos-Sacchi, On the frequency limit and phase of outer hair cell motility: Effects of the membrane filter. *J. Neurosci.* **12**, 1906–1916 (1992).
49. D. Z. He, P. Dallos, Properties of voltage-dependent somatic stiffness of cochlear outer hair cells. *J. Assoc. Res. Otolaryngol.* **1**, 64–81 (2000).
50. A. Altoe, C. Shera, Nonlinear cochlear mechanics without direct vibration-amplification feedback. *Phys. Rev. Research* **2**, 013218 (2020).
51. J. Cormack, Y. Liu, J. H. Nam, S. M. Gracewski, Two-compartment passive frequency domain cochlea model allowing independent fluid coupling to the tectorial and basilar membranes. *J. Acoust. Soc. Am.* **137**, 1117–1125 (2015).